

Supporting Information

**Intrinsic Nanoscale Structure of Thin Film Composite
Polyamide Membranes: Connectivity, Defects, and
Structure-Property Correlation**

Xiaoxiao Song ^{a, b*}, Bowen Gan ^a, Saren Qi ^c, Hao Guo ^d, Chuyang Y. Tang ^{d*}, Yong
Zhou ^{a, b}, Congjie Gao ^{a, b}

^a Centre for Membrane Separation and Water Science & Technology, Department of Chemical
Engineering, Zhejiang University of Technology, Hang Zhou, 310014, P. R. China

^b Collaborative Innovation Center of Membrane Separation and Water Treatment of Zhejiang
Province, Hangzhou 310014, China

^c Suzhou Institute of Nano-Tech and Nano-Bionics (SINANO), Chinese Academy of Sciences,
Suzhou 215123, P. R. China

^d Department of Civil Engineering, the University of Hong Kong, Pokfulam, Hong Kong SAR, P. R.
China

* To whom all correspondence should be addressed.

Xiaoxiao Song Tel: +86 (0571) 8832 4135, E-mail address: songxiaoxiao@zjut.edu.cn

Chuyang Y. Tang Tel: +852 2859 1976, Fax: +852 2559 5337, E-mail address: tangc@hku.hk

This SI contains 20 pages, with 10 figures and 2 tables.

22	<u>Table of Contents</u>	
23		
24	S1. Membrane performance tests	Page S3
25	S2. The impact of NaOCl treatment on the PSF substrate	Page S4
26	S3. FESEM micrographs of the exterior features of XLE and NF90	Page S6
27	S4. Determination of nodule size	Page S7
28	S5. Determination of the apparent and intrinsic thicknesses by TEM	Page S8
29	S6. Determination of SAR value using TEM micrographs	Page S10
30	S7. Fe(II) tracer filtration test from the backside of BW30	Page S11
31	S8. HA tracer filtration tests from the frontside of BW30 and NF90	Page S14
32	S9. FESEM observation of the defective nodular layer of NF90	Page S17
33	S10. XPS elemental composition of the frontside and backside of	
34	isolated PA layers	Page S18
35	S11. Effect of DMF treatment on PA morphology	Page S19
36		
37	References	Page S20
38		

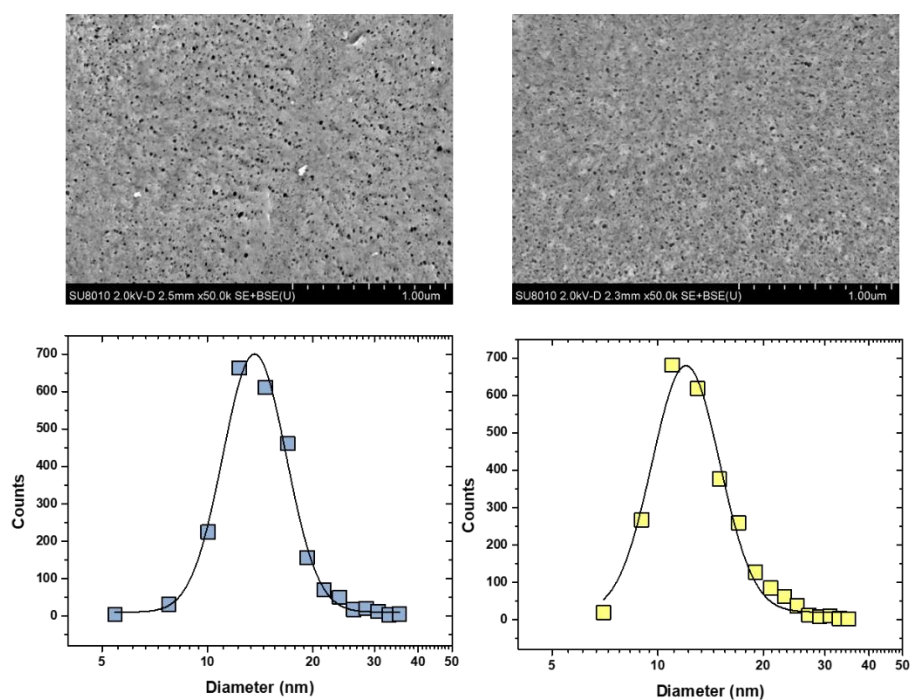
S1. Membrane performance tests

A customized cross-flow membrane setup was equipped with a Hydracell pump (model D-03, Minneapolis, MN) and multiple stainless steel filtration cells arranged in parallel.^{1, 2} Each test cell has an effective diameter of 5.2 cm and a feed channel depth of ~ 1.2 mm. The testing solution temperature was maintained constant at 25 ± 1 °C with a recirculation water bath. NaCl rejection and water flux was tested at both low salinity (2,000 ppm NaCl under a pressure of 1.6 MPa and a cross flow of 2 L/min) and high salinity (32,000 ppm NaCl, under a pressure of 5.5 MPa and a cross flow of 3 L/min). NaCl rejection was evaluated based on conductivity measurements of the feed and permeate water, and water flux was determined by weighing the mass of permeate in accordance to our previous publication.^{2, 3}

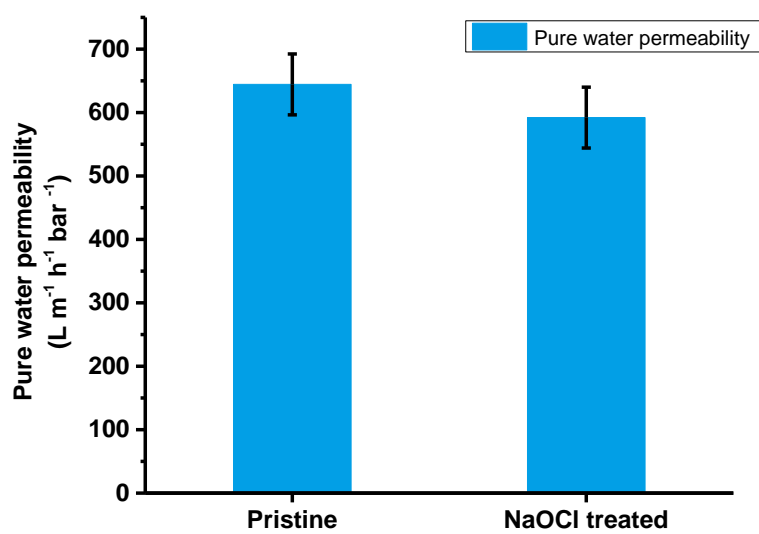
S2. The impact of NaOCl treatment on the PSF substrate

In order to study the effect of NaOCl treatment method on the size distribution of the PSF substrate, PSF membrane coupons were soaked in 1% NaOCl solution for 30 h. The pore sizes were counted in ImageJ software. Results show that the NaOCl treatment had no obvious effect on the pore size distribution (Figure S1a).

The permeability of the pristine and the NaOCl treated PSF membranes were evaluated at an applied pressure of 0.1 MPa. Before data collection, the membranes were pre-conditioned at the same pressure for 40 minutes. Each test was repeated for 3 times using different membrane coupons. The water permeability before and after the NaOCl treatment were $644.4 \pm 48.0 \text{ L m}^{-2} \text{ h}^{-1}$ and $592.2 \pm 48.0 \text{ L m}^{-2} \text{ h}^{-1} \text{ bar}^{-1}$, respectively (Figure S1b). The difference was comparable to the standard deviation for the permeability measurements, suggesting that the changes caused by the NaOCl treatment was insignificant.



(a) non-treated PSF sub. NaOCl treated (30 h) PSF sub.



(b)

Figure S1. The impact of NaOCl treatment on the PSF substrate. (a) Pore size analysis of PSF substrates without NaOCl treatment (left) and with NaOCl treatment (right, soaked in 1% NaOCl at pH=12 for 30 hours). (b) Pure water permeability of PSF substrates before and after NaOCl treatment.

S3. FESEM micrographs of the exterior features of XLE and NF90

As shown in Figure S2, the exterior PA layers of XLE and NF90 are composed of overlapping flat features (circled by dotted red line). The nodules underneath the exterior layers are exposed through the crater-like “apertures”.

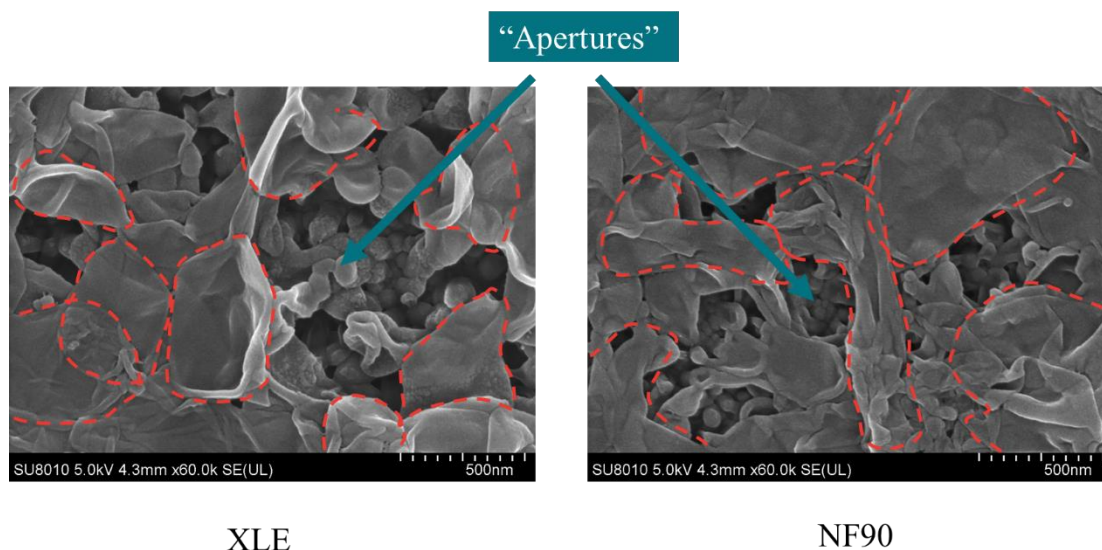


Figure S2. FESEM images of the exterior features of XLE and NF90.

S4. Determination of nodule size

The size of nodules was determined based on the cross-sectional FESEM images of the membranes. Figure S3 shows an example for the measurement of nodular size of XLE, where lines are drawn to represent the widest span of each nodule. The reported nodular size is the average of at least 10 counts at different locations.

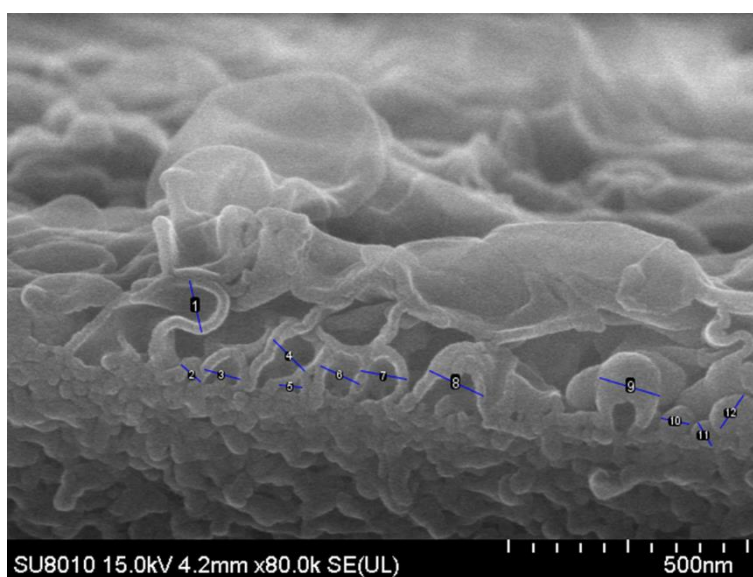


Figure S3. Measurement of the sizes of the nodules in the nodular layer of XLE membrane. Length of the marked lines was measured using the ImageJ software.

S5. Determination of the apparent and intrinsic thicknesses of polyamide layers

Apparent thickness, δ_{app} , was determined based on the average of the thicknesses of at least 10 locations in the TEM cross-section of a membrane. At each location, the thickness was measured by the vertical span from the bottom of the nodular layer to the frontside of the polyamide layer. The measured δ_{app} values followed the order of XLE (277 ± 43 nm) > NF90 (159 ± 27 nm) > SW30HR (129 ± 61 nm) > BW30 (118 ± 58 nm). The large standard deviations were caused by the significant spatial variations in δ_{app} . For example, the apparent thickness of SW30HR and BW30 was ~200 nm at some locations where large leaf-like features were present, but its value was much smaller (~ 50 nm) at other locations where leaves were absent. This variation was probably caused by non-uniform degassing conditions. An earlier study⁴ further revealed that the leaf-like features were formed due to the deformation of large inflated nodules upon drying.

As an alternative method, the apparent thickness of the polyamide rejection layer can also be determined as the ratio of the apparent cross-sectional area (including the voids) over the width of the polyamide layer section. For XLE shown in Figure S4a, the area of the polyamide section is 387,106 nm² and the projected width of PA is 1,319 nm, which yields an apparent thickness of 293 nm. This value agrees well with the value obtained by sampling the thickness at multiple locations (277 ± 43 nm), which suggests that the average value calculated from the multiple locations can well

represent δ_{app} .

The intrinsic thickness, δ_{int} , was determined by the average nodular wall thickness of at least 10 random locations. Figure S4b shows the measurement of δ_{int} using membrane XLE as an example. The intrinsic layer thicknesses of all membranes are in the range of 10 - 20 nm.

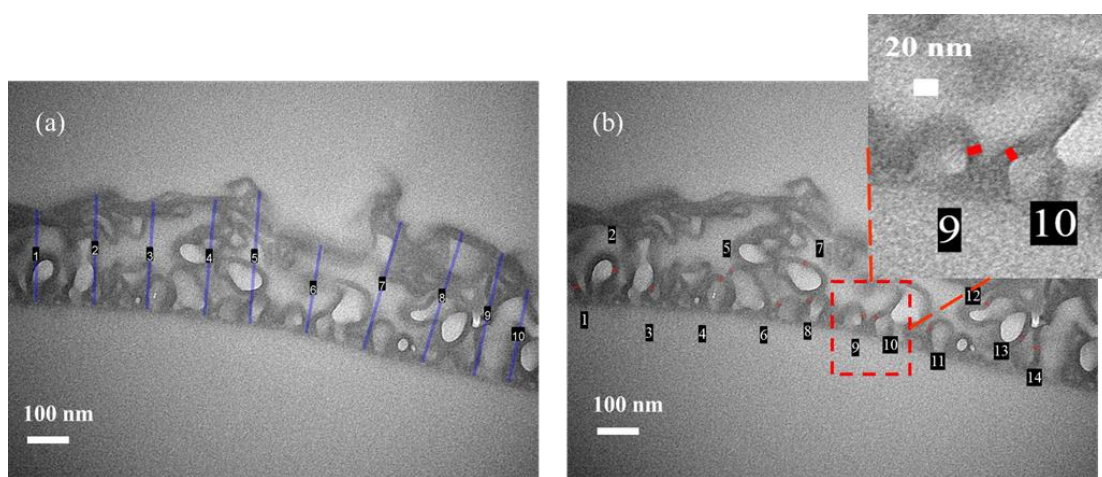


Figure S4. The measurement of (a) the δ_{app} (as marked by blue lines) and (b) the δ_{int} (as marked by red lines) of the PA layer of XLE membrane based on a TEM cross-sectional micrograph.

S6. Determination of SAR value using TEM micrographs

To determine the SAR value, a typical TEM cross-section was selected (Figure S5).

The image was converted to binary black and white format, showing the PA layer in

black color. The ImageJ software was used to count the total number pixels in black

color. Since the size of the pixel can be calibrated by the scale bar of the micrograph

(length of scale bar/number of pixels in the direction of the scale bar), the

cross-sectional area of the PA (X_{PA}) can be determined from the number of pixels.

Assuming a thickness of δ_{PA} (normal to the cross-section), the volume occupied by the

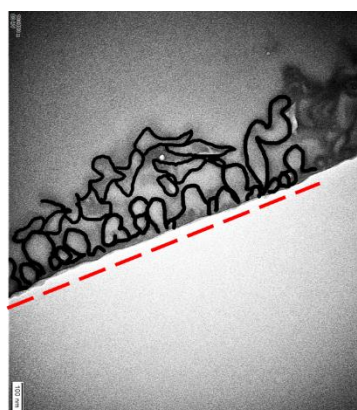
PA is given by $X_{PA}\delta_{PA}$. Consequently, the surface area of PA is then calculated by the

volume of PA divided by the average intrinsic thickness of PA film ($X_{PA}\delta_{PA}/\delta_{int}$). On

the other hand, the projected area of the PA film is given by the length of the baseline

l_{base} in the TEM image (see marked by the dotted red line in Figure S5) times δ_{PA} . As

such, the SAR value is given by: $SAR = (X_{PA}\delta_{PA}/\delta_{int})/(l_{base}\delta_{PA}) = X_{PA}/(\delta_{int}l_{base})$.



$$X_{PA} = 117153.4 \text{ nm}^2$$

$$\delta_{int} = 13.9 \text{ nm}$$

$$l_{base} = 1195.7 \text{ nm}$$

$$SAR = 7.05$$

Figure S5. The derivation of SAR value from the TEM image for XLE membrane.

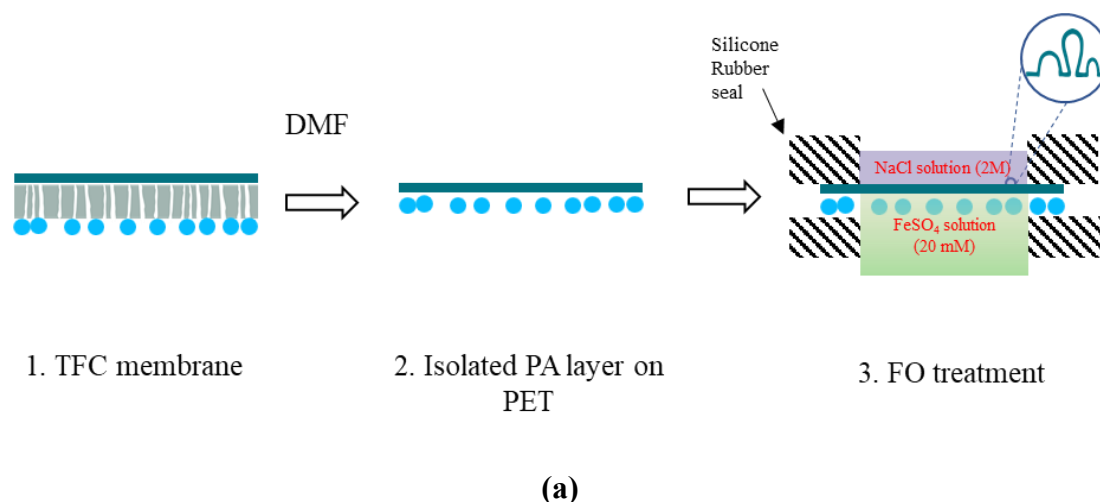
The area occupied by dark black lines represent the cross-sectional area of PA. Red

dotted line represents the length of baseline. Scale bar = 100 nm.

S7. Fe(II) tracer filtration test from the backside of BW30

Fe(II) tracer filtration test was conducted for the BW30 membrane. Compared to HA macromolecules, the dissolved nature of Fe^{2+} allows it to better penetrate the nanosized pores and thus determine the salt-discriminating layer. In addition, the iron-based tracer can offer better contrast for TEM characterization. To complement the HA tracer tests, we performed the Fe(II) tracer test under forward osmosis, which avoids the application of hydraulic pressure from the backside. The PA layer of a BW30 membrane was isolated from its PSF substrate (by dissolving PSF in a DMF solution) to reduce the effect of internal concentration polarization. During the isolation process, the isolated PA layer floated to the surface of the DMF solution. Continuous supply of fresh DMF solution from a pipette to the isolated PA layer dissolved away the residue PSF. Then, the transparent isolated PA layer was picked up by the PET fabric from the bottom. During the isolation process, the isolated PA layer was maintained facing up. Therefore, the frontside of the PA layer was away from the PET and the backside of the PA layer was towards the PET (Figure S6a). This isolated PA layer, supported on the PET fabric, was clamped between two pieces of round silicon rubber frame (inner diameter $\sim 3\text{cm}$) with the frontside of PA facing upward. A 20 mM FeSO_4 solution was supplied to the PET side. Subsequently, a 2 M NaCl solution was introduced to the frontside of the PA layer to induce an osmotic flow of water from the FeSO_4 solution to the 2 M NaCl solution. This operation was continued for 3 hours, during which the NaCl solution was refreshed at approximately

every 20 minutes to maintain the osmotic flow. This osmotic flow delivered Fe(II) to the backside of the polyamide layer and penetrate into its nanovoids (Figure S6b), confirming that the frontside skin of membrane is the salt-discriminating layer.



TEM image

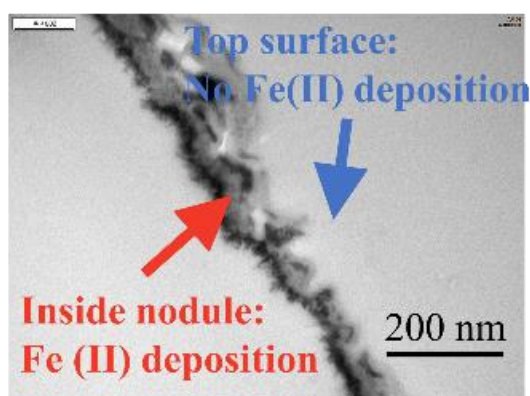


Figure S6: Fe(II) tracer filtration test from the backside of BW30. (a) Schematic diagram showing the isolation of the PA layer and the setting up of the tracer test. A FeSO₄ solution was delivered to the backside of an isolated PA layer (supported on PET) under an osmotically induced flux using a 2 M NaCl solution. (b) TEM micrograph of the PA layer after the tracer test. Fe(II) accumulated inside the porous

167 part of the PA layer and subsequently precipitated as $\text{Fe}(\text{OH})_3$ (the black-colored
168 material in the TEM image) in the presence of O_2 .
169

S8. HA tracer filtration tests from the frontside of BW30 and NF90

Results of HA tracer filtration tests from the frontside of membrane BW30 and NF90 were obtained from our previous study.⁵ Specifically, the filtration was performed in a cross-flow filtration setup^{1, 5} using a feed solution containing 5 mg/L HA, 1mM CaCl₂ and 7mM NaCl under constant pressure (200 psi for BW30 and 100 psi for NF90) over 24 hours. Figures S7 and S8 present some previously unpublished TEM micrographs.

As shown in Figure S7, the HA macromolecules were nearly completely rejected by the nodular layer of the BW30 membrane, possibly due to a more intact PA film and/or the presence of its polyvinyl alcohol surface coating layer⁶. On the other hand, the HA macromolecules could partially intrude into the nodules of the NF90 PA layer (highlighted by the dotted circle), indicating the presence of possible defects in the NF90 nodular layer. TEM micrographs at higher magnification further show that the HA macromolecules penetrated in the PSF substrate of NF90 (indicated by the red arrows in Figure S8).

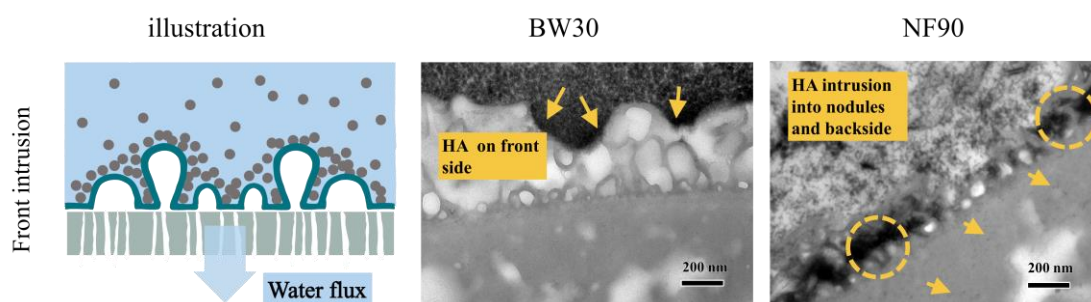


Figure S7. Illustration of HA tracer filtration tests from the frontside of a PA layer

(left panel) and TEM micrographs of BW30 and NF90 after the tracer tests (right panel).

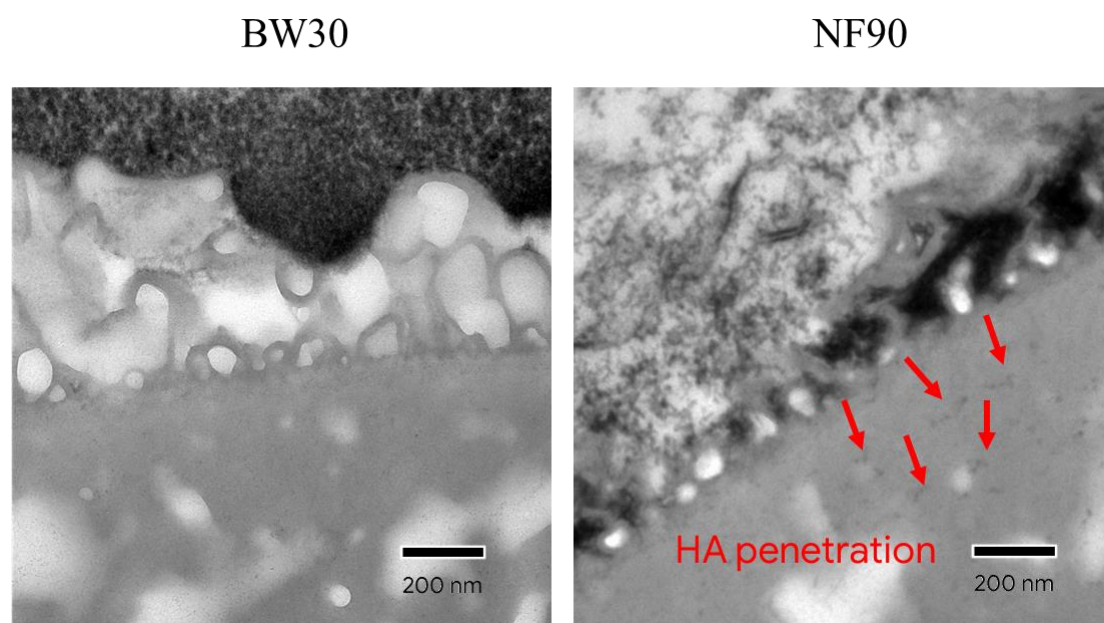
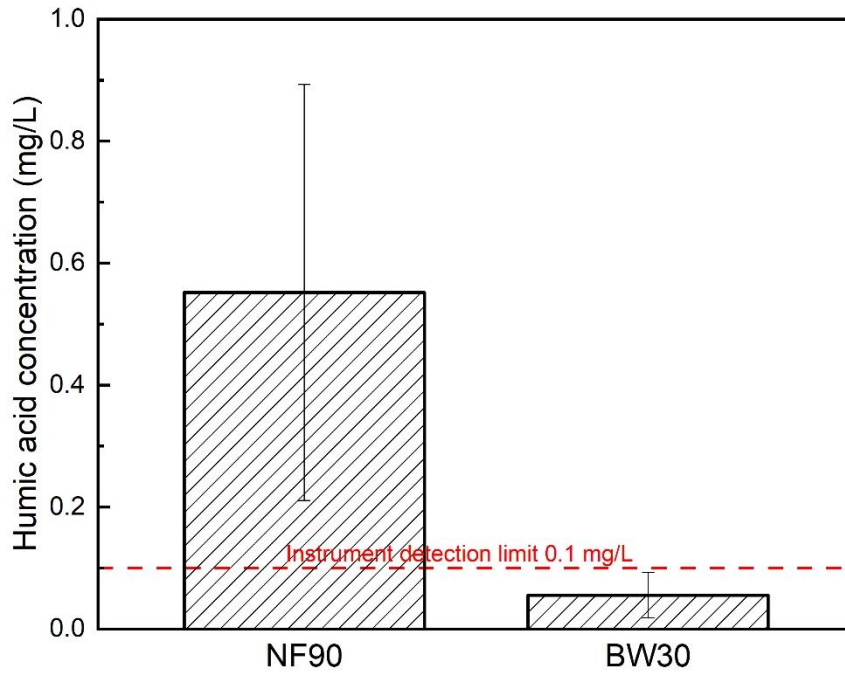


Figure S8. High magnification TEM micrographs of BW30 and NF90 after HA tracer filtration tests from the frontside.

To further confirm the presence of defects in NF90, we performed HA rejection tests for NF90 and BW30 using a feed water containing 50 mg/L HA at pH 7. The applied pressure was adjusted to achieve an initial flux of approximately $20 \text{ L m}^{-2} \text{ h}^{-1}$ for both membranes. The concentration of HA in the permeate water was determined by total organic carbon measurements. While the concentration of HA in the permeate of BW30 was below the detection limit (0.1 mg/L), HA appeared in the permeate of NF90 (Figure S9), which supports our hypothesis that defects exist for NF90.



203

204 Figure S9. Humic acid concentration in the permeate water. The feed water contained

205 50 mg/L HA at pH 7. Permeate samples were collected at 15 minutes after the

206 addition of HA in the feed water to minimize the effect of fouling on HA transport

207 through the membranes. For each membrane type, the reported results were based on

208 three different membrane coupons.

S9. FESEM observation of the defective nodular layer of NF90

Defects of various sizes can be frequently observed on the skins of the PA nodules of membrane NF90 (Figure S9).

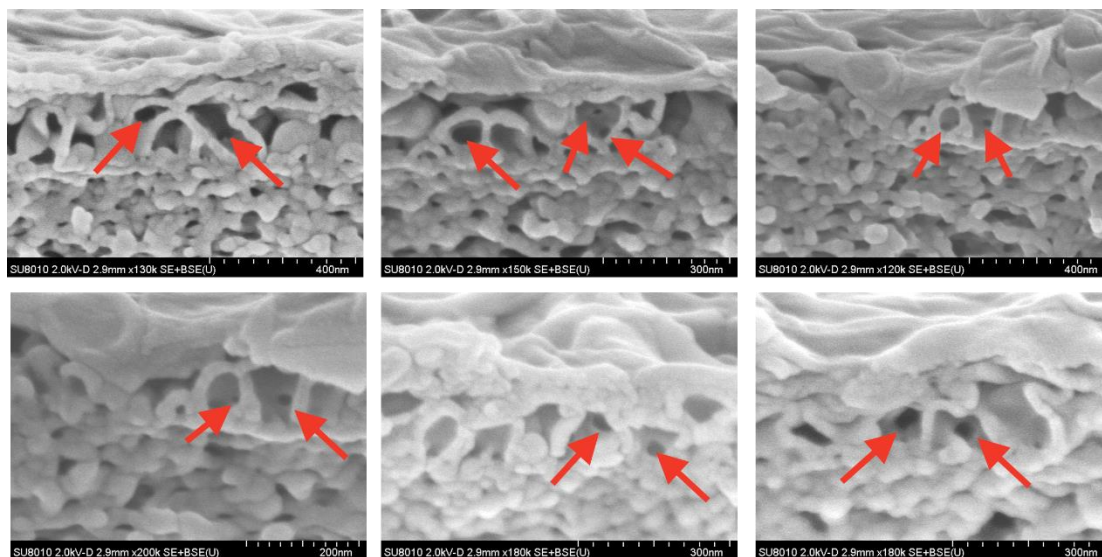


Figure S10. Representative cross-sectional FESEM images of the PA layer of NF90 membrane.

215 **S10. XPS elemental composition of the frontside and backside of isolated PA layers**

216 Table S1 shows the XPS elemental composition of the frontside and backside of PA layers isolated from the four commercial membranes. The
 217 O/N ratio cannot be calculated for the frontside PA of SW30HR and BW30 due to the presence of an O-rich PVA surface coating for these
 218 membranes.⁶

219 Table S1. The XPS analysis of the membranes

	%O	%N	%C	%Cl	O/N of polyamide
SW30HR (front)	23.9 ± 1.5	5.9 ± 1.5	70.1 ± 0.6	0.15 ± 0.05	N.A.
SW30HR (back)	13.6 ± 0.9	12.3 ± 0.3	73.9 ± 0.9	0.16 ± 0.05	1.10 ± 0.08
BW30 (front)	27.6 ± 1.2	3.9 ± 0.9	68.5 ± 0.4	0.00 ± 0.00	N.A.
BW30 (back)	13.1 ± 0.4	12.6 ± 0.3	72.9 ± 0.6	0.15 ± 0.04	1.04 ± 0.04
XLE (front)	17.7 ± 1.0	11.9 ± 0.6	70.3 ± 1.2	0.18 ± 0.05	1.50 ± 0.12
XLE (back)	13.0 ± 0.5	12.1 ± 0.5	73.5 ± 1.0	0.36 ± 0.35	1.07 ± 0.07
NF90 (front)	17.0 ± 0.5	12.5 ± 0.6	70.4 ± 1.0	0.12 ± 0.03	1.36 ± 0.05
NF90 (back)	12.8 ± 0.4	12.6 ± 0.5	74.5 ± 0.4	0.12 ± 0.04	1.01 ± 0.06

220

S11. Effect of DMF treatment on PA morphology

The isolation of PA layer by DMF treatment is commonly used in the literature⁷⁻¹⁰ and have been shown not to affect the physiochemical and transport properties of the polyamide layer.^{10, 11} In Table S2, we compare the surface roughness of PA films of BW30 before and after isolation. Our results show no significant change in PA morphology.

Table S2. AFM surface roughness of PA films of BW30 before and after isolation

Roughness Parameter	Original PA ^a		Isolated PA (after DMF wash) ^b	
	Average	Standard deviation	Average	Standard deviation
R_a (nm)	36.0	1.4	37.4	3.2
R_q (nm)	45.6	2.3	47.5	3.6
R_{max} (nm)	355	38	435	91

Notes:

a. based on measurements of 5 membrane samples;

b. based on measurements of 5 isolated PA layers.

References

- (1) Tang, C. Y.; Fu, Q. S.; Robertson, A. P.; Criddle, C. S.; Leckie, J. O. Use of Reverse Osmosis Membranes to Remove Perfluorooctane Sulfonate (PFOS) from Semiconductor Wastewater. *Environ. Sci. Technol.* 2006, 40 (23), 7343-7349.
- (2) Liu, L.; Xie, X.; Qi, S.; Li, R.; Zhang, X.; Song, X.; Gao, C. Thin film nanocomposite reverse osmosis membrane incorporated with UiO-66 nanoparticles for enhanced boron removal. *J. Membr. Sci.* 2019, 580, 101-109.
- (3) Song, X.; Qi, S.; Tang, C. Y.; Gao, C. Ultra-thin, multi-layered polyamide membranes: Synthesis and characterization. *Journal of Membrane Science* 2017, 540, 10-18.
- (4) Song, X.; Gan, B.; Yang, Z.; Tang, C. Y.; Gao, C. Confined nanobubbles shape the surface roughness structures of thin film composite polyamide desalination membranes. *Journal of Membrane Science* 2019, 582, 342-349.
- (5) Tang, C. Y.; Kwon, Y.-N.; Leckie, J. O. Fouling of reverse osmosis and nanofiltration membranes by humic acid—Effects of solution composition and hydrodynamic conditions. *J. Membr. Sci.* 2007, 290 (1), 86-94.
- (6) Tang, C. Y.; Kwon, Y.-N.; Leckie, J. O. Probing the nano- and micro-scales of reverse osmosis membranes—A comprehensive characterization of physiochemical properties of uncoated and coated membranes by XPS, TEM, ATR-FTIR, and streaming potential measurements. *J. Membr. Sci.* 2007, 287 (1), 146-156.
- (7) Lin, L.; Feng, C.; Lopez, R.; Coronell, O. Identifying facile and accurate methods to measure the thickness of the active layers of thin-film composite membranes – A comparison of seven characterization techniques. *J. Membr. Sci.* 2016, 498, 167-179.
- (8) Lin, L.; Lopez, R.; Ramon, G. Z.; Coronell, O. Investigating the void structure of the polyamide active layers of thin-film composite membranes. *J. Membr. Sci.* 2016, 497, 365-376.
- (9) Freger, V. Swelling and morphology of the skin layer of polyamide composite membranes: An atomic force microscopy study. *Environ. Sci. Technol.* 2004, 38 (11), 3168-3175.
- (10) Lee, J.; Doherty, C. M.; Hill, A. J.; Kentish, S. E. Water vapor sorption and free volume in the aromatic polyamide layer of reverse osmosis membranes. *J. Membr. Sci.* 2013, 425-426, 217-226.
- (11) Bason, S.; Oren, Y.; Freger, V. Ion transport in the polyamide layer of RO membranes: Composite membranes and free-standing films. *J. Membr. Sci.* 2011, 367 (1), 119-126.